Experimental verification of orbital engineering at the atomic scale: Charge transfer and symmetry breaking in nickelate heterostructures

Patrick J. Phillips, Xue Rui, Alexandru B. Georgescu, Ankit S. Disa, Paolo Longo, Eiji Okunishi, Fred Walker, Charles H. Ahn, Sohrab Ismail-Beigi, and Robert F. Klie

Phys. Rev. B **95**, 205131 — Published 19 May 2017

DOI: 10.1103/PhysRevB.95.205131

Experimental verification of orbital engineering at the atomic scale: charge transfer and symmetry breaking in nickelate heterostructures

Patrick J. Phillips, Xue Rui, and Robert F. Klie

Nanoscale Physics Group, University of Illinois at Chicago, Chicago, IL 60607

Paolo Longo

Gatan Inc., Pleasanton, CA 94588

Alexandru B. Georgescu, Ankit S. Disa, Fred Walker, Sohrab Ismail-Beigi, and Charles H. Ahn

Department of Physics, Department of Applied Physics, and Center for Research on Interface Structures and Phenomena (CRISP), Yale University, New Haven, CT 06511

Eiji Okunishi

JEOL Ltd., Tokyo 196-8558, JAPAN

(Dated: April 27, 2017)

Abstract

Epitaxial strain, layer confinement and inversion symmetry breaking have emerged as powerful new approaches to control the electronic and atomic-scale structural properties in complex metal oxides. Trivalent rare-earth (RE) nickelate $RENiO_3$ heterostructures have been shown to be exemplars since the orbital occupancy, degeneracy, and, consequently, the electronic/magnetic properties can be altered as a function of epitaxial strain, layer thickness and superlattice structure. One recent example is the tri-component $LaTiO_3$-$LaNiO_3$-$LaAlO_3$ superlattice which exhibits charge transfer and orbital polarization as the result of its interfacial dipole electric field. A crucial step towards control of these parameters for future electronic and magnetic device applications is to develop an understanding of both the magnitude and range of the octahedral network's response towards interfacial strain and electric fields. An approach that provides atomic-scale resolution and sensitivity towards the local octahedral distortions and orbital occupancy is therefore required. Here, we employ atomic-resolution imaging coupled with electron spectroscopies and first principles theory to examine the role of interfacial charge transfer and symmetry breaking in a tricomponent nickelate superlattice system. We find that nearly complete charge transfer occurs between the $LaTiO_3$ and $LaNiO_3$ layers, resulting in a mixed Ni^{2+}/Ni^{3+} valence state. We further demonstrate that this charge transfer is highly localized with a range of about 1 unit cell within the $LaNiO_3$ layers. We also show how Wannier-function-based electron counting provides a simple physical picture of the electron distribution that connects directly with formal valence charges. The results presented here provide important feedback to synthesis efforts aimed at stabilizing new electronic phases that are not accessible by conventional bulk or epitaxial film approaches.

PACS numbers:

Keywords: nickelate, scanning transmission electron microscopy, orbital engineering, electron energy-loss spectroscopy

I. INTRODUCTION

For many technologically relevant materials systems, in particular transition-metal oxides (TMOs), the orbital structure (relative energies, filling, etc.) directly correlates to the material's resulting properties.[1–5] For example, systems such as the manganites (colossal magnetoresistance),[6] the cobaltates (spin-state transitions),[7,8] and the cuprates (high-temperature superconductivity)[9,10] owe their behaviors to specific configurations of the electronically active transition-metal cation d orbitals, which, for near-cubic symmetry, are split into the (lower energy) t_{2g} and (higher energy) e_g orbitals. The development of atomically precise growth techniques for oxides has opened up the possibility of controlling orbital configurations via layered heterostructures.

Ni^{3+} (d^7) is a d orbital open-shell system, with fully occupied t_{2g} orbitals and a single electron occupying the twofold-degenerate e_g manifold given cubic symmetry. $LaNiO_3$ (LNO), possessing a pseudocubic perovskite structure, is a material recently explored in the context of orbital engineering, with the goal of breaking its orbital degeneracy and emulating the single-band structure of the cuprates.[11–13] A recent publication on a $LaTiO_3$-$LaNiO_3$-$LaAlO_3$ (LTNAO) superlattice demonstrated the successful breaking of this e_g orbital degeneracy by using atomic-layer synthesis to alter its symmetry and filling; an approximately 50% change in the occupation of the Ni e_g orbitals was reported[14] and verified via X-ray absorption spectroscopy and *ab initio* theory, confirming the creation of an electronic configuration which approaches a single-band Fermi surface.

The three-component superlattice, where 1 unit cell (uc) of $LaTiO_3$ (LTO) and 1 uc of LNO are sandwiched between 3 uc of $LaAlO_3$ (LAO) develops a large orbital polarization as a result of an inherent inversion symmetry breaking, internal charge transfer, and the emergent ionic polarization.[14,15] This effect is based on the transfer of a single electron from the LTO layer to the LNO layer due to the mismatch in electronegativity of the two cations. The electron transfer creates a dipole field which leads to large polar distortions with polarization pointing towards the NiO_2 layer of the LNO. The combination of these polar distortions and the symmetry breaking of the superlattice about the LNO layer results in asymmetric stretching of the NiO_6 oxygen octahedra, leading to a large crystal field splitting and a polarization in the orbital occupations which resembles the arrangement in the high-temperature superconducting cuprates. Prior work[14] infers the charge transfer

from the spatially-averaged X-ray absorption spectroscopy (XAS) measurements on the Ti L-edgeand Ni L-edge.

In this work, we focus on a specific superlattice system, consisting of 1 uc of LTO, 2 uc of LNO and 3 uc of LAO. We aim to directly measure the proposed charge transfer and determine its spatial range using this superlattice. More specifically, we utilize aberration-corrected scanning transmission electron microscopy (STEM) coupled with both energy dispersive X-ray (EDX) and electron energy loss (EEL) spectroscopies to quantify the charge transfer and symmetry breaking at the atomic scale. We directly map the charge transfer with STEM EELS/EDX, providing direct evidence for the key driving force of orbital polarization in the three-component system. Furthermore, we detect the signatures of orbital polarization in this LTNAO superlattice with atomic resolution, as previously suggested by sample-averaged experiments. Additionally, we perform first principles density functional theory (DFT)[16,17] simulations within the local density approximation (LDA)[18] to simulate and verify basic aspects of the electronic structure of these heterostructures.

It should be noted that an analysis with the spatial and chemical resolution as presented here would not be have been possible without recent instrumentation and software advances: this work requires an imaging probe which has a high enough current density to generate appreciable X-ray signals yet is also able to achieve sub-Å spatial resolution. Electron microscopy has a rich history in the advanced characterization of oxides, for example, in the atomic-scale imaging of composition, bonding, electron spatial distribution at interfaces, valence determination, etc.[19–26] By taking advantage of the numerous imaging and spectroscopy modes on advanced aberration-corrected instruments, it is feasible to locally conduct a complete chemical, structural, and electronic characterization at the atomic scale. The high/low angle annular dark field (H/LAADF) and annular bright field (ABF) STEM signals can be simultaneously acquired, resulting in images which are sensitive to atomic number, strain, and light element contrast, respectively.[27–30] In terms of spectroscopy, both EDX and EEL signals can be simultaneously acquired, thereby providing atomically-resolved chemical and electronic information.

II. METHODS

A. Thin Film Synthesis

The tricomponent superlattice is grown on $LaAlO_3$ (001) single crystal substrates using oxygen plasma assisted molecular beam epitaxy. The layering sequence for superlattice is $[(LTO)_1$-$(LNO)_2$-$(LAO)_3]\times$ 12 with a total film thickness of ≈28 nm. Each layer is grown via co-deposition of the respective elements. The growth is monitored in situ by reflection high energy electron diffraction (RHEED). Post-growth RHEED images display sharp narrow streaks indicative of coherent epitaxy. Ex situ atomic force microscopy reveals low surface roughness (≈1-2 Å) and unit cell high (≈4 Å) steps post-growth. More details on the thin film growth can be found in Ref. 14

B. X-ray Absorption Spectroscopy

XAS measurements shown in Figures 3(b) and 4(b) were carried out at beamline $U4B$ at the National Synchrotron Light Source. Spectra were recorded in total electron yield mode and normalized by the incident flux as measured by an upstream Au mesh. The energy of the Ti L- and O K-edges were calibrated with reference to a simultaneously measured TiO_2 powder. A linear background is subtracted from the data by fitting to the pre-edge region ≈ 5-10 eV below the edge.

C. First-Principles Modeling

We performed first principles calculations using Density Functional Theory (DFT) with ultrasoft pseudopotentials[31–33] using the Quantum Espresso software.[34] To approximate the effects of exchange-correlation, we used the local density approximation (LDA)[18] along with a +U correction for the $3d$ transition metal atomic orbitals.[35] For Ni, we choose U=0 which is the best available DFT approach for describing bulk LNO,[36] while for Ti we use U=8 eV which provides a sensible band alignment between titanates and LNO.[14,15,37] k-point sampling of the Brillouin zone employed a mesh equivalent to a $12 \times 12 \times 12$ mesh for a 5-atom pseudocubic bulk unit cell. Band occupations were Gaussian broadened with width 0.03 eV. The plane wave cutoff was 35 Ryd for the wave functions and 280 Ryd for the

electron density. Structural relaxations were terminated when all components of atomic forces are below 0.03 eV/Å in magnitude. The simulated superlattices, $(LNO)_1$-$(LNO)_2$-$(LAO)_3$, were periodic in all directions and biaxially strained to the theoretically computed pseudocubic lattice parameter of $LaAlO_3$ at 3.71 Å. Superlattices with $c\,(2 \times 2)$ interfacial unit cells were simulated allowing for octahedral rotations and tilts. We generate Maximally Localized Wannier Functions[38,39] using the Wannier90 software.[40]

D. Scanning Transmission Electron Microscopy

Combined atomic EELS and EDS data were acquired using a cold-field emission gun JEOL GrandARM 60-300 kV, operated at 160 kV with a beam current of about 85 pA. The microscope is equipped with dual large solid-angle SDD detectors for the acquisition of EDS data and a Gatan GIF Quantum ER for the acquisition of EELS data. EELS data was acquired in DualEELS mode where both the the low- and core-loss spectra were acquired simultaneously. The zero-loss peak, present in the low-loss spectra, can be used to correct and remove all the effects of energy drift allowing a more accurate measurement of any chemical shift. The EELS spectrometer was setup with a dispersion of 0.1 eV / channel resulting in an energy resolution of 0.5 eV that was needed in order to resolve all the spectral features present in the EELS spectrum moving across the super lattice layers. For simultaneous high-angle annular dark field (HAADF) and annular bright field (ABF) imaging, a probe-convergence angle of 25 mrad was used with a inner detector angle and angular range of 12 mrad for ABF and an inner detector angle of 55 mrad for HAADF imaging.

Chemical and electronic analyses have made great strides in recent years, owing largely to high-area silicon drift EDX detectors and high-speed/high-sensitivity EEL spectrometers.[41][42] Simultaneous acquisition of both signals allows one to avoid the high energy edges in EELS (La, Ni, and Al in this case) in favor of a higher energy dispersion, and to rely on EDX to identify the remaining elements. The higher energy dispersion in EELS then enables the detailed near-edge fine structure analysis of relevant energy loss, including the Ti L- and O K-edge.

III. RESULTS AND DISCUSSION

Figure 1 presents a STEM overview of the superlattice structure, following a focused ion beam (FIB) preparation; note that not all the superlattice repeats are visible, as the topmost section of the sample has been milled away in order to render the remainder of the sample sufficiently thin for STEM analysis. Figures 1(a,b) provide a low magnification view of the structure in both LAADF and ABF modes, which reveal some regions of localized strain (anomalously bright/dark in LAADF/ABF), likely from the presence of occasional dislocations; this localized strain is in addition to the strain associated with the superlattice, evidenced by the layering in both the LAADF and ABF images. It is very difficult to discern the identity of the individual layers exclusively via imaging, as there is very little Z-contrast gradient across the interfaces of LAO-LTO-LNO (Figure 1(c)); thus, chemical spectroscopy is required. As LAADF/ABF are considerably less sensitive to atomic number contrast, there is no reason other than epitaxial strain (the forced constraint on the lattice parameters) for the obvious contrast between layers in Figures 1(a,b,d).

Several integrated signals are presented in Figure 2, coming from both EELS and EDX. More specifically, Figure 2(a) shows the spectrum images for the simultaneously-acquired Ti L- and O K-edges using EELS and the Ni and Al K-, as well as the La L-edges using EDX integrated intensities. The atomic columns in each layer of the superlattice are clearly resolved according to the structural model shown Figure 2(b). While we do not observe significant interdiffusion for most elements of the superlattice, it appears that some Ti signal is also measured in the adjacent LNO layer (e.g., columns Ni-2a). We will return to this point in our discussion of Figure 4(a) and 4(c). The La spectrum images shows a slight gradient in column intensity (from left to right), which is associated with local variations in the sample thickness, potentially due to preferential ion milling during the sample preparation steps. Therefore, the La intensity is used to normalize the O K-edge signal in Figure 2(a), and we can clearly see that the oxygen concentration remains constant across the different superlattice layers. Note that the average O K-edge signal refers to the vertically integrated signal between the La atomic columns to exclude signal variations due to the La atomic columns during normalization. Figure 2(b) shows the structural model for the LTNAO superlattice including the expected distortions of the oxygen octahedra, as well as an RGB image of the transitions metal chemical makeup of the LTNAO superlattice

structure. The labels for the different Ti and Ni layers are also shown. It is important to point out here that each pixel in the spectrum images shown in Figure 2 contains an entire EELS or EDX spectrum. The discussion following below will focus on the detailed analysis of the EELS fine-structures for the different atomic columns within the LTNAO superlattices.

Figure 3(a) shows the Ti L-edge signal averaged over the column labeled Ti-2 (Figure 3(c)). The EELS near-edge fine-structure of the Ti L-edges exhibits four distinct peaks, which are commonly associated with the Ti^{4+} valence state,[19] since they result from the splitting of the degenerate $3d$ final states into the t_{2g} and e_g levels for each of the Ti L_2 and L_3 edges.[20] This is in contrast to bulk LTO, where we have Ti^{3+} (d^1), which has a less well-defined t_{2g}-e_g splitting and a markedly different Ti L-edge fine-structure — all of which is easily identified via EELS.[19] That we have Ti^{4+} in the LTNAO superlattice is the first piece of direct evidence of the desired donation of an e^- from Ti: the presence of Ti^{4+} is consistent with XAS measurements, which average over the entire superlattice film (see Figure 3(b)). XAS has the advantage of higher energy resolution than EELS but provides little spatial resolution. A comparison of the EELS Ti L-edges taken from the LTO layers and from bulk $SrTiO_3$, which contains Ti^{4+}, is shown in the Supplemental Materials,[43] demonstrating that the fine-structures of the Ti in LTNAO is identical to the one expected for a Ti^{4+} valence state. Unfortunately, extracting the Ni valence in the LNO layers via a similar analysis of the Ni L-edge is not possible here due to the nearly complete overlap between the La M- and the Ni L-edges. In what follows below, we will instead focus on the O K-edge analysis to extract and quantify the interfacial charge transfer. We emphasize here that the observed change in Ti valence is not due to film stoichiometry, i.e. oxygen vacancies. As discussed above, after accounting for local variations in the sample thickness, it can be seen in Figure 2(a) that the oxygen stoichiometry for all three layers remains unchanged, and we also find that the O K-edge EEL spectra from the $LaAlO_3$ layers (which can be considered as a bulk reference in this context) show the fine structure expected for stoichiometry $LaAlO_3$. Therefore, it appears that all layers in the superlattice are stoichiometric and the observed changes in the valence and EELS fine-structure are associated only with interfacial charge transfer.

Various O K-edge spectra are provided for the Ti and Ni columns contained within the spectroscopic region of interest, again integrating a number of rows, along the respective

columns (Figure 4). While there are some differences in the absolute intensity of the main peak, we will be focusing on the pre-peak of the O K-edge, which results from electronic transitions into the hybridized O $2p$ - transition metal (TM) $3d$ orbitals.[44] What is visible in all the spectra is a pre-peak centered around 530 eV (labeled A), and an additional peak near 528 eV (B), which is only present in the spectra from the Ni columns. Indeed, XAS of the O K-edge (Figure 4(b)) confirms the presence of both of these pre-peaks, A and B. We reiterate that XAS is a spatially averaging spectroscopic technique and cannot tell us the specific spatial origin of these peaks. These peaks are readily explained by comparison to known bulk EEL spectra, shown in Figure 4(d). Looking at bulk LTO (Ti^{3+}), we see merely a slight pre-shoulder on the main peak due to its $3d^1$ configuration and a decreased number of unoccupied states. In STO, which has Ti^{4+} and a $3d^0$ configuration, a strong pre-peak intensity (A) is seen. Peak A in the Ti column of the LTNAO superlattice is analogous to that seen in the STO as opposed to the LTO bulk reference, again showing that we have Ti^{4+} in the superlattice. The reference spectrum for bulk LNO (Figure 4(d)) with Ni^{3+} shows a pre-peak B at 528 eV which is lower in energy than those of LTO and STO, which have edge onset energies of 532 eV and 530 eV (A), respectively. In the superlattice, the lower energy pre-peak B at 528 eV is only seen in the Ni columns and has strongly reduced intensity compared to bulk LNO. We attribute this to the fact that the Ni layers have accepted an e^- from Ti and thus the degree of Ni^{3+} character is greatly suppressed in the superlattice. The intensity reduction agrees with prior literature[45], which also has shown that the degree of covalency between Ni and O is reduced upon electron doping.

Looking carefully at peak A in all of the spectra shown in Figures 4(a) and (c), there is still significant spectral weight in both Ni columns. Given that there is some Ti is present in the first Ni column of each superlattice (based on the EELS/EDX spectroscopy), some of the intensity in peak A can potentially be explained by remnant Ti contributions. However, when examining the O K-edge fine-structure of La_2NiO_4 (Figure 4(d)) which has Ni^{2+} valence, we do not find any sign of the pre-peak B at 528 eV (unlike Ni^{3+} in $LaNiO_3$ reference), but instead a shoulder at $\approx$530 eV, which coincides with the position of peak A in Figure 4(c). Hence, the peak A intensity in the superlattice spectra is not completely due to the remnant Ti contributions but also due to the contribution of Ni^{2+}.

It is interesting to note that the intensity of peak A is significantly higher in the layer closest to LTO (i.e. Ni-1a and Ni-2a) and decreases in the layers closest to LAO (i.e. Ni-1b

and Ni-2b). Without further insights from theoretical modeling, it is impossible to disentangle the contributions to this peak stemming from remnant Ti^{3+} in the LNO layer closest to LTO and from the increasing Ni valence in the layer closest to the LAO layers. We acknowledge that with our electron probe in a channeling condition (i.e., a zone axis orientation), we must be cautious when attempting quantitative EELS and EDX measurements, as these experiments can be convoluted by elastic and thermal diffuse scattering of the incident electrons.[46,47] However, in the case of the present fine structure analysis, we are simply looking at clear trends in the spectra, which appear and disappear rapidly, generally within a single unit cell, as shown in Figure 4(a); we furthermore note the good agreement the XAS data, which is insensitive to channeling.

For our DFT calculations, we simulated the LTNAO superlattice as well as the reference systems NiO (nominally Ni^{2+}), bulk $LaNiO_3$ (nominally Ni^{3+}), bulk $LaTiO_3$ (nominally Ti^{3+}), and bulk $SrTiO_3$ (nominally Ti^{4+}). We calculate the relaxed LDA atomic-scale structures, orbital occupancies and the O K-edge spectra using both the Z and Z+1 approximations.[4849] The most informative comparison between theory and experiment comes from the calculated electron counts of the 3d orbitals displayed in Table I.

We have used two different localized basis sets to compute the orbital occupancies since each basis is suited to a different experimental measurement. The first basis set is the 3d atomic orbitals (pseudo-atomic orbitals of the pseudopotential). These are relevant for describing highly localized, atomic-like physics: e.g., XAS or EELS core excitation spectra are most readily understood as transitions from core to valence atomic orbitals. For LTNAO, this is the most appropriate basis for describing the Ni orbital polarization.[14] The second basis set is Wannier functions generated to describe the conduction band states of each metal oxide system: a set of localized orbitals of 3d symmetry centered on the transition metals that *exactly* span the Hilbert space of conduction bands near the Fermi level. These Wannier functions are designed to count band occupancy and thus formal valence (see the Supplementary Materials[43] for band structures, densities of states, and orbital occupancies).

Table I displays significant differences between the two bases: the atomic orbital occupancies are quite large and nowhere near what one expects based on chemical intuition or formal electron counting. The Wannier occupancies reproduce the formal valence in the reference compounds and provide a straightforward description of the electron distribution. For example, in the Wannier basis for LTNAO, the net electron count on the one Ti and

two Ni sums up to exactly 15 as per formal charge counting. The atomic orbital basis does not obey any simple sum rule. Hence, we use the Wannier basis for valence quantification and the atomic basis to compute orbital polarization.

The data in Table I describes an LTNAO electron distribution concordant with the above observations: the Ti is essentially fully ionized to Ti^{4+}, the Ni-a column closest to the LTO receives most of the transferred electron (0.60 e^-) with the remainder going to the farther Ni-b (0.35 e^-). This uneven distribution is sensible since the donated electron is attracted to the now positively charged TiO_2 layer and thus prefers to reside primarily on the Ni-a. The more strongly doped Ni-a has significant orbital polarization (hole ratio r deviating from unity) while Ni-b is much less orbitally polarized (see the Supplementary Material[43] for detailed densities of states and orbital occupancies).

Due to the difference in valence on Ni-a and Ni-b, we would expect the O K-edge spectra to differ for these two Ni layers in the LTNAO. The comparison to bulk references (Figure 4(d)) had shown that the energy of pre-peak A ($\approx$ 530 eV) primarily corresponds to $Ti^{4+/3+}$ and Ni^{2+} while the energy of pre-peak B ($\approx$ 528 eV) corresponds primarily to Ni^{3+}. Based on the theoretical Ni valences, we expect the intensity ratio of peaks A and B to be larger for the LNO adjacent to LTO (i.e., Ni-1a and Ni-2a) than for the second LNO layer (Ni-1b and Ni-2b), reflecting the stronger Ni^{2+} character. This prediction is in agreement with the experimental measurements and confirmed by integrating peak A and B intensities for the LTO, two Ni-a, and two Ni-b columns. The average A/B-peak ratio decreases as expected: 5.24 (Ti), 3.26 (Ni-a), and 2.56 (Ni-b), demonstrating the larger amount of Ni^{2+} character in the Ni column adjacent to LTO.

We note that, despite much effort, a direct comparison of EELS data to theoretically calculated O K-edge spectra did not produce any useful agreement of the energies or intensities of the peaks for bulk LNO or LTNAO. Hence, we do not rely on them in our theoretical analysis. Given that DFT is a ground state theory, it can, in principle, correctly compute the mean electron distribution and orbital occupations. However, as is well known, using DFT to predict electronic excitations (such as EELS) is much more problematic. Furthermore, localized dynamical electronic correlations are not included in DFT band structures, further degrading comparisons to experiments in correlated complex oxides. We have, therefore, focused on using the observables that should be predicted correctly by DFT: mean electron occupations.

IV. CONCLUSIONS

In summary, by combining atomically-resolved energy-loss and X-ray data with first principles DFT calculations, direct evidence is provided of the charge transfer from LTO into LNO in tricomponent superlattices. Using the high spatial sensitivity of STEM imaging and electron spectroscopies, we confirm previous XAS measurements, which have reported a ≈50 % change in the orbital occupation that is significantly higher (by a factor of 2-3) compared to previous results.[50] Furthermore, we demonstrate that this interfacial charge transfer from the LTO to the LNO layers is highly localized in real space and is mainly limited to the layers directly adjacent to each other. The range of the interfacial charge transfer is of the order of 1 unit-cell or about 4 Å. These types of results and analysis provide crucial feedback for future orbitally selective synthesis methods, where the magnitude and range of charge transfer and orbital polarization will be used to stabilize novel electronic phases inaccessible by conventional epitaxial methods.

Acknowledgements

PJP and RFK acknowledge funding from the National Science Foundation (NSF) via Grant Number DMR-1408427 to support this work. Work at Yale supported by NSF MRSEC DMR-1119826 (CRISP) and AFOSR under grant number FA95501510472. Use of the National Synchrotron Light Source at Brookhaven National Lab was supported by the Office of Science, Office of Basic Energy Sciences, of the US Department of Energy under Contract No. DE-AC02-98CH10886.

[1] A. V. Boris, Y. Matiks, E. Benckiser, A. Frano, P. Popovich, V. Hinkov, P. Wochner, M. Castro-Colin, E. Detemple, V. K. Malik, et al., Science **332**, 937 (2011).

[2] J. Chakhalian, J. M. Rondinelli, J. Liu, B. A. Gray, M. Kareev, E. J. Moon, N. Prasai, J. L. Cohn, M. Varela, I. C. Tung, et al., Physical Review Letters **107**, 116805 (2011).

[3] A. Frano, E. Schierle, M. W. Haverkort, Y. Lu, M. Wu, S. Blanco-Canosa, U. Nwankwo, A. V. Boris, P. Wochner, G. Cristiani, et al., Physical Review Letters **111**, 106804 (2013).

[4] D. P. Kumah, A. S. Disa, J. H. Ngai, H. H. Chen, A. Malashevich, J. W. Reiner, S. Ismail-Beigi, F. J. Walker, and C. H. Ahn, Advanced Materials **26**, 1935 (2014).

[5] R. Scherwitzl, S. Gariglio, M. Gabay, P. Zubko, M. Gibert, and J. M. Triscone, Physical Review Letters **106**, 246403 (2011).

[6] Y. Tokura and Y. Tomioka, Journal of Magnetism and Magnetic Materials **200**, 1 (1999).

[7] G. Maris, Y. Ren, V. Volotchaev, C. Zobel, T. Lorenz, and T. T. M. Palstra, Physical Review B **67**, 224423 (2003).

[8] R. F. Klie, J. C. Zheng, Y. Zhu, M. Varela, J. Wu, and C. Leighton, Physical Review Letters **99**, 047203 (2007).

[9] L. F. Feiner, M. Grilli, and C. DiCastro, Physical Review B **45**, 10647 (1992).

[10] E. Pavarini, I. Dasgupta, T. Saha-Dasgupta, O. Jepsen, and O. K. Andersen, Physical Review Letters **87**, 047003 (2001).

[11] J. Chaloupka and G. Khaliullin, Physical Review Letters **100**, 016404 (2008).

[12] P. Hansmann, X. Yang, A. Toschi, G. Khaliullin, O. K. Andersen, and K. Held, Physical Review Letters **103**, 016401 (2009).

[13] A. S. Disa, F. J. Walker, S. Ismail-Beigi, and C. H. Ahn, APL Materials **3**62303 (2015).

[14] A. S. Disa, D. P. Kumah, A. Malashevich, H. Chen, D. A. Arena, E. D. Specht, S. Ismail-Beigi, F. J. Walker, and C. H. Ahn, Physical Review Letters **114**, 026801 (2015).

[15] H. H. Chen, D. P. Kumah, A. S. Disa, F. J. Walker, C. H. Ahn, and S. Ismail-Beigi, Physical Review Letters **110**186402 (2013).

[16] P. Hohenberg and W. Kohn, Phys. Rev. **136**, B864 (1964).

[17] W. Kohn and L. J. Sham, Phys. Rev. **140**, A1133 (1965).

[18] J. P. Perdew and A. Zunger, Physical Review B **23**, 5048 (1981).

[19] A. Ohtomo, D. A. Muller, J. L. Grazul, and H. Y. Hwang, Nature **419**, 378 (2002).

[20] L. F. Kourkoutis, H. L. Xin, T. Higuchi, Y. Hotta, J. H. Lee, Y. Hikita, D. G. Schlom, H. Y. Hwang, and D. A. Muller, Philosophical Magazine **90**, 4731 (2010).

[21] D. A. Muller, L. F. Kourkoutis, M. Murfitt, J. H. Song, H. Y. Hwang, J. Silcox, N. Dellby, and O. L. Krivanek, Science **319**, 1073 (2008).

[22] A. Gulec, P. J. Phillips, and R. F. Klie, Applied Physics Letters **107**, 143111 (2015).

[23] M. Varela, M. P. Oxley, W. Luo, J. Tao, M. Watanabe, A. R. Lupini, S. T. Pantelides, and S. J. Pennycook, Physical Review B **79**, 085117 (2009).

[24] L. Laffont and P. Gibot, Materials Characterization **61**, 1268 (2010).

[25] N. Gauquelin, E. Benckiser, M. K. Kinyanjui, M. Wu, Y. Lu, G. Christiani, G. Logvenov, H. U. Habermeier, U. Kaiser, B. Keimer, et al., Physical Review B **90**, 195140 (2014).

[26] M. K. Kinyanjui, Y. Lu, N. Gauquelin, M. Wu, A. Frano, P. Wochner, M. Reehuis, G. Christiani, G. Logvenov, H. U. Habermeier, et al., Applied Physics Letters **104**, 221909 (2014).

[27] E. J. Kirkland, R. F. Loane, and J. Silcox, Ultramicroscopy **23**, 77 (1987).

[28] R. F. Loane, P. Xu, and J. Silcox, Ultramicroscopy **40**, 121 (1992).

[29] P. J. Phillips, M. De Graef, L. Kovarik, A. Agrawal, W. Windl, and M. J. Mills, Ultramicroscopy **116**, 47 (2012).

[30] S. Findlay, N. Shibata, H. Sawada, E. Okunishi, Y. Kondo, and Y. Ikuhara, Ultramicroscopy **110**, 903 (2010).

[31] D. Vanderbilt, Physical Review B **41**, 7892 (1990).

[32] K. Laasonen, R. Car, C. Lee, and D. Vanderbilt, Phys. Rev. B **43**, 6796 (1991).

[33] K. Laasonen, A. Pasquarello, R. Car, C. Lee, and D. Vanderbilt, Phys. Rev. B **47**, 10142 (1993).

[34] P. Giannozzi, et al., Journal of Physics: Condensed Matter **21**, 395502 (2009).

[35] V. I. Anisimov, F. Aryasetiawan, A. I. Lichtenstein, Journal of Physics: Condensed Matter **9**, 767 (1997).

[36] G. Gou, I. Grinberg, A. M. Rappe, and J. M. Rondinelli, Phys. Rev. B **84**, 144101 (2011).

[37] M. S. J. Marshall, A. Malashevich, A. S. Disa, M.-G. Han, H. Chen, Y. Zhu, S. Ismail-Beigi, F. J. Walker, C. H. Ahn, Physical Review Applied **2**, 051001 (2014).

[38] N. Marzari, D. Vanderbilt, Physical Review B **56**, 12847 (1997).

[39] I. Souza, N. Marzari, D. Vanderbilt, Physical Review B **65**, 035109 (2001).

[40] A. Mostofi, J. Yates, Y.-S. Lee, I. Souza, D. Vanderbilt, N. Marzari, Computer Physics Com-

munications **178**, 685 (2008).

[41] L. J. Allen, A. J. D'Alfonso, B. Freitag, and D. Klenov, MRS Bulletin **37**, 47 (2012).

[42] P. J. Phillips, T. Paulauskas, N. Rowlands, A. W. Nicholls, K.-B. Low, S. Bhadare, and R. F. Klie, Microscopy and Microanalysis **20**, 1046 (2014).

[43] See supplemental material at [url will be inserted by publisher] for more details on the first-principles modeling and EELS fine-structure.

[44] M. Abbate, F. M. F. de Groot, J. C. Fuggle, A. Fujimori, O. Strebel, F. Lopez, M. Domke, G. Kaindl, G. A. Sawatzky, M. Takano, et al., Physical Review B **46**, 4511 (1992).

[45] J. Suntivich, W. T. Hong, Y.-L. Lee, J. M. Rondinelli, W. Yang, J. B. Goodenough, B. Dabrowski, J. W. Freeland, and Y. Shao-Horn, The Journal of Physical Chemistry C **118**, 1856 (2014).

[46] N. R. Lugg, M. Haruta, M. J. Neish, S. D. Findlay, T. Mizoguchi, K. Kimoto, and L. J. Allen, Applied Physics Letters **101**, 183112 (2012).

[47] N. R. Lugg, M. J. Neish, S. D. Findlay, and L. J. Allen, Microscopy and Microanalysis **20**, 1078 (2014).

[48] R. A. Tilton, D. J. Phelps, C. P. Flynn, Physical Review Letters **32**, 1006 (1974).

[49] R. Buczko, G. Duscher, S. J. Pennycook, S. T. Pantelides, Physical Review Letters **85**, 2168 (2000).

[50] M. Wu, E. Benckiser, M. W. Haverkort, A. Frano, Y. Lu, U. Nwankwo, S. Brueck, P. Audehm, E. Goering, S. Macke, et al., Physical Review B **88**, 125124 (2013).

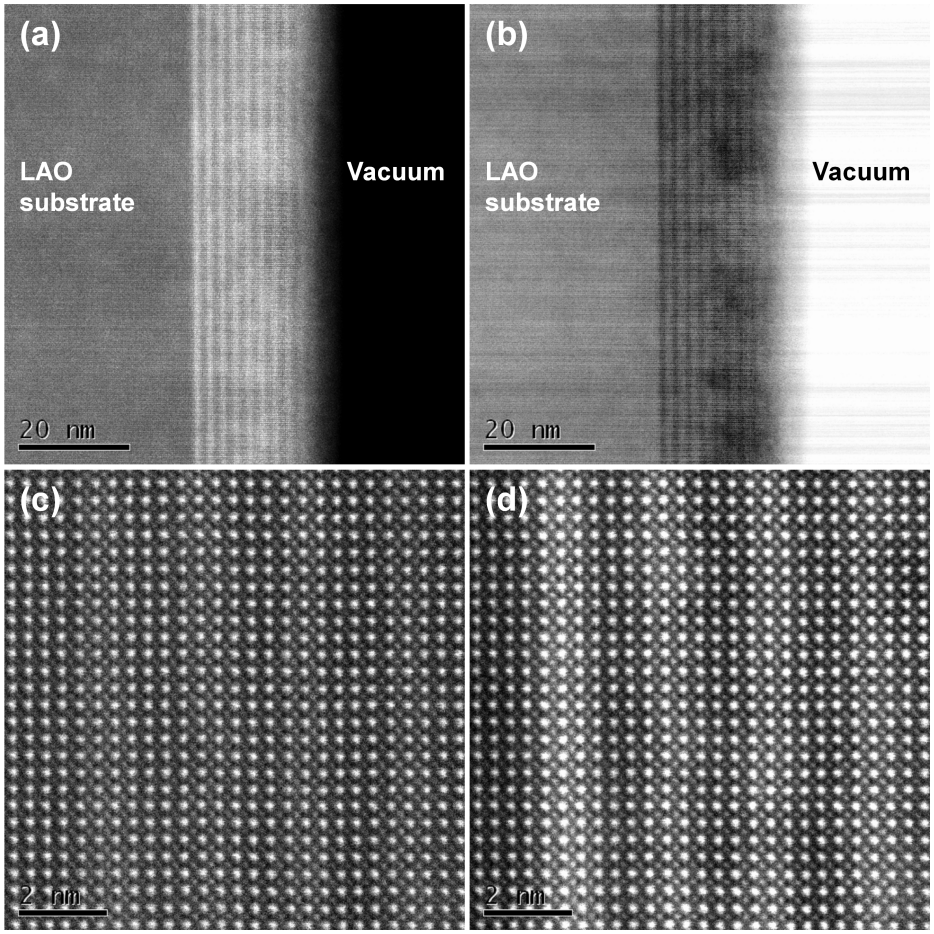

FIG. 1: (a,b) Low magnification LAADF/ABF image pair of the superlattice structure, with the film growth direction to the right. Some strain is obvious in structure, and the occasional dislocation is observed. These areas were avoided for all chemical and electronic analysis; (c,d) Higher magnification HAADF/LAADF images showing the (lack of) Z-contrast and again, the strain contrast.

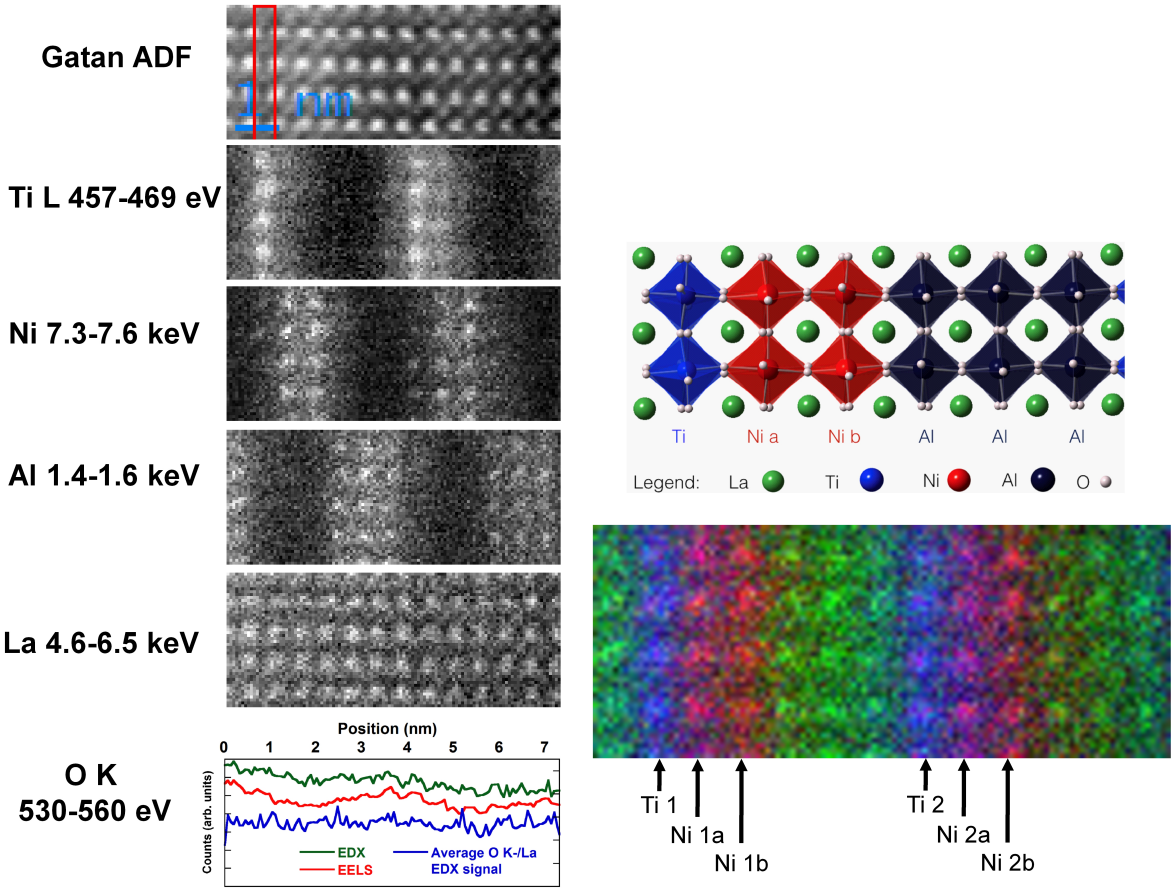

(a) (b)

FIG. 2: (a) Spectroscopic analysis of the two superlattice repeats, shown in conjunction with all relevant chemical signals obtained either by integrating the EELS or EDX signals. The vertically integrated O K-edge signal is shown as a line-profile for the EELS and EDX signals, as well as the O K-edge EDX signal normalized with respect to the La signal to account for thickness variations from ion milling. (b) Top: Structural model of the superlattice. Bottom: Combined spectrum image using the EELS Ti L-edge (blue), EDX Ni K- edge (red) and EDX Al K-edge signals, respectively.

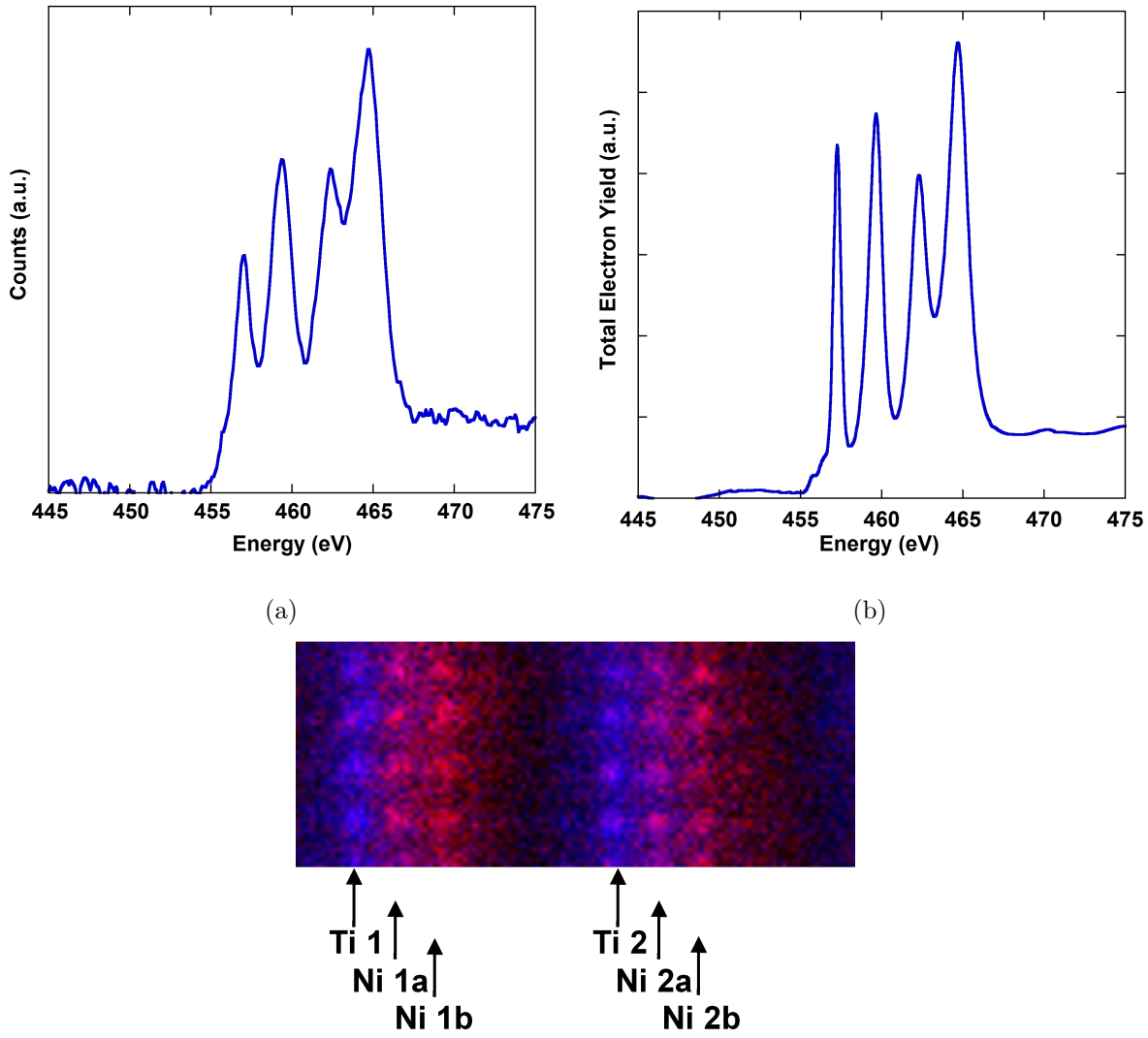

FIG. 3: (a) Electron energy-loss and (b) X-ray absorption (right) spectra for the Ti L-edge. In the case of EELS, the spectrum was acquired by integrating (vertically) column Ti-2 as shown in (c). (c) Atomic-resolution spectrum image showing the transition metal oxide atomic columns in the $LaTiO_3$ (blue) and $LaNiO_3$ (red) layers.

System	Site	Atomic d orbitals		Wannier orbitals	
		d occupancy	Hole ratio, r	d occupancy	Valence
$SrTiO_3$	Ti	2.83	–	0.00	+4.00
$LaTiO_3$	Ti	2.58	–	1.00	+3.00
NiO (Ni^{2+})	Ni	8.70	1	8.00	+2.00
$LaNiO_3$ (Ni^{3+})	Ni	8.64	1	7.00	+3.00
LTNAO	Ti	2.77	–	0.05	+3.95
	Ni-a	8.73	0.56	7.60	+2.40
	Ni-b	8.67	0.91	7.35	+2.65

TABLE I: LDA+U calculated d manifold occupations, hole ratio $r = h_{3z^2-r^2}/h_{x^2-y^2}$, and valence state for bulk references and the superlattice (h_i is the hole occupation of orbital i).

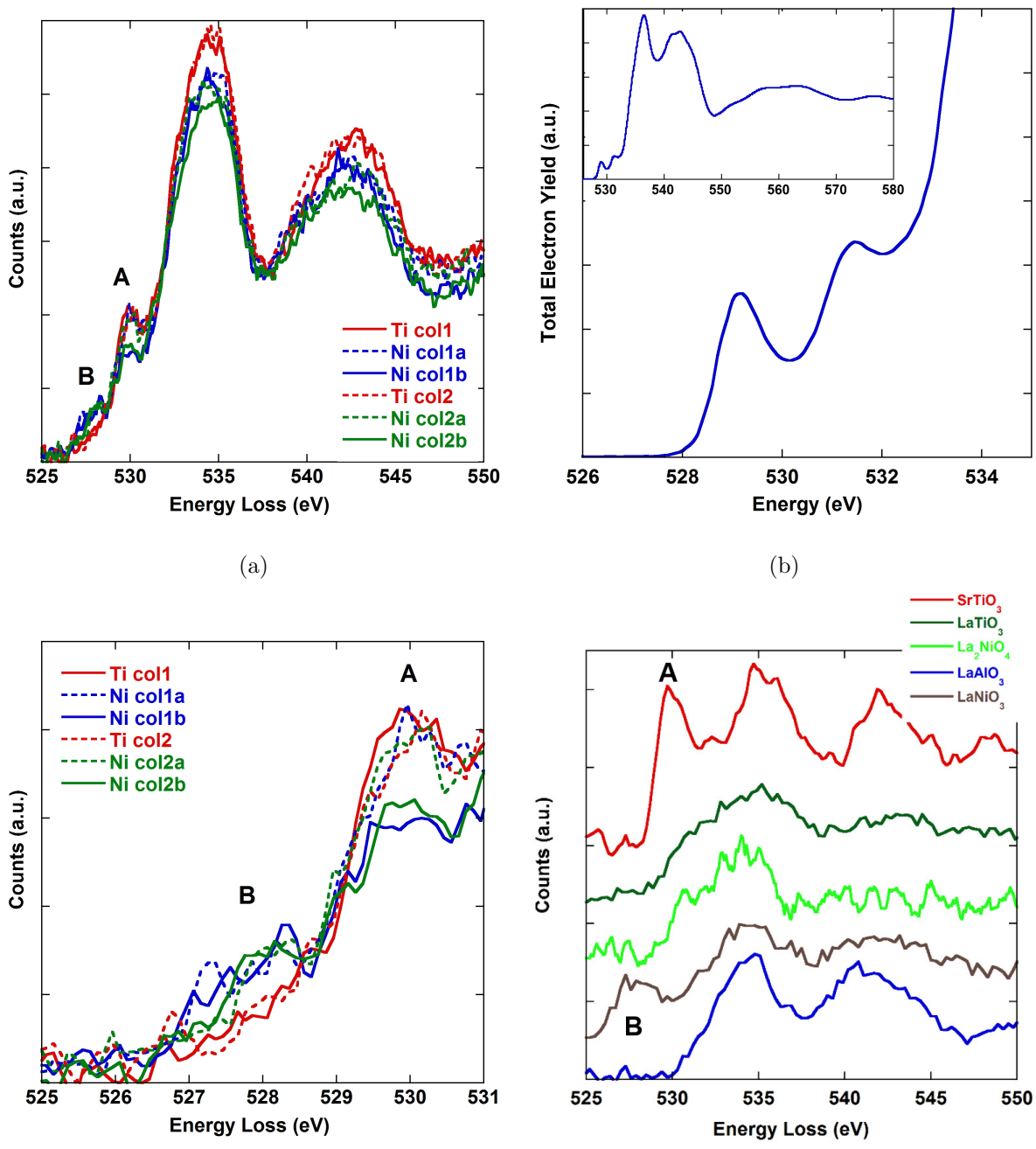

FIG. 4: O K-edge spectra: (a) EEL spectra integrated (vertically) over the atomic columns indicated in Figure 2(a). (b) X-ray absorption spectrum of the entire superlattice film; the inset shows an overview of a larger energy range. (c) magnified pre-peak region shown in (a) for the $LaTiO_3$ and $LaNiO_3$ layers with the different pre-peaks labeled A and B. (d) Reference spectra for Ti^{4+} ($SrTiO_3$), Ti^{3+} ($LaTiO_3$), Ni^{3+} ($LaNiO_3$), Ni^{2+} (La_2NiO_4) and $LaAlO_3$.